Title

Mechanism of Exact Transition between Cationic and Anionic Redox Activities in Cathode Material Li2FeSiO4

Journal

The Journal of Physical Chemistry Letters, 9(21)

ISSN

1948-7185

Authors

Zheng, Jiaxin
Teng, Gaofeng
Yang, Jinlong
et al.

Publication Date

2018-11-01

DOI

10.1021/acs.jpclett.8b02725

Peer reviewed

Exact transition between cationic and anionic redox activities in cathode materials

Jiaxin Zheng[1, #], Gaofeng Teng[1, #], Jinlong Yang[1, #], Ming Xu[1], Zengqing Zhuo[1,2], Wanli Yang[2], Qihang Liu[3,4*] and Feng Pan[1,*]

[1]School of Advanced Materials, Peking University, Shenzhen Graduate School, Shenzhen 518055, People's Republic of China.

[2]Advanced Light Source, Lawrence Berkeley National Laboratory, Berkeley, CA 94720, United States.

[3]Department of Physics, South University of Science and Technology of China, Shenzhen 518055, China

[4]University of Colorado, Boulder, Colorado 80309, United States

[#]These authors contributed equally to this work.

*Corresponding author: qihang.liu85@gmail.com and panfeng@pkusz.edu.cn

Abstract

The discovery of anion redox activity is promising for boosting the capacity of lithium-ion battery (LIB) cathodes. However, fundamental understanding of the mechanisms that trigger the anionic redox is still lacking. Here, using hybrid density functional study combined with experimental soft X-ray absorption spectroscopy (sXAS) measurements, we unambiguously proved that $Li_{(2-x)}FeSiO_4$, a widely-studied cathode material for LIBs, performs sequent cationic and anionic redox activity through delithiation. Specifically, Fe^{2+} is oxidized to Fe^{3+} during the first Li-ion extraction per formula unit (f.u.), while the second Li-ion extraction triggered the oxygen redox exclusively. The transition between cationic and anionic redox activities happens exactly at $LiFeSiO_4$, with electron and hole polaronic behaviors, respectively. For other polyanionic transition-metal (TM) materials in this family, while Li_2NiSiO_4 shows similar sequent redox activity as Li_2FeSiO_4, Li_2MnSiO_4 shows the multiple cationic redox (Mn^{2+}-Mn^{4+}) during the whole delithiation, and Li_2CoSiO_4 shows a simultaneous cationic and anionic redox. The present finding not only provides new insights into the oxygen redox activity in polyanionic compounds for rechargeable batteries, but also sheds light on the future design of high-capacity rechargeable batteries.

Introduction

Charge compensation of transition metals (TM) in TM-based compounds when the total charge of the compound is altered (e. g., through oxidation/reduction, carrier injection, chemical doping) is a fundamental and intriguing topic both in physics and chemistry [1]. Classic inorganic chemistry tacitly assumes that most of the changes of the total charge are accommodated by a change in the charge of the TM ion [2,3]. Typically, for rechargeable lithium-ion batteries (LIBs) cathode materials, TM-ions were regarded as the sole sources of electrochemical activity in an intercalation cathode to provide the charge-compensating electrons after Li-ion extraction [4-8]. For example, when $LiTMO_2$ is fully delithiated, the original TM^{3+} ion is thought to be oxidated to a TM^{4+} ion. As a result, the theoretical capacity of these oxides has been limited by the number of electrons offered by the TM redox reaction and its relatively high atomic weight.

Until recently, this scenario is challenged by the discovery of anionic redox activity in Li-rich layered TM oxides [9-18], such as layered NMC (Ni–Mn–Co) [14,19,20], Li_2MnO_3 [21-23], $Li_{1.2}Ni_{0.2}Mn_{0.6}O_2$ [24], $Li_{1.3}Mn_{0.4}Nb_{0.3}O_2$ [25], $Li_{1.3}Nb_{0.3}Me_{0.4}O_2$ (Me=Fe^{3+}, Mn^{3+} and V^{3+}) [26], $Li_2Ru_{1-y}Sn_yO_3$ [9,12], Li_4FeSbO_6 [11], Li_8ZrO_6 [27], α-Li_2IrO_3 [10], β-Li_2IrO_3 [16], and Li_3IrO_4 [28]. Recently, the discovery of anionic redox activity has been

extended to other kinds of cathode materials beyond Li-rich layered TM oxides, such as non-layered TM oxides (e. g., rock-salt-type $Li_4Mn_2O_5$ and Li_5FeO_4) [29,30] and metal–organic compounds (e. g., CuTCNQ) [31]. Anionic reduction not only extends our understanding of the charge compensation process during delithiation in cathodes, but also raises the opportunity to boost the capacity and energy density of LIBs by combining both cationic (transition metal) and anionic (oxygen) redox processes within the same material [13,32,33].

However, such staggering capacities suffer from capacity fade with cycling [28], which is mainly due to the irreversible loss of lattice oxygen during the anionic redox process [14,18,34]. Thus, clarifying the specific redox mechanism and fundamental understanding of the local structure and electronic state evolutions during anionic redox process, which are closely associated with the stability of the lattice oxygen and the reversibility of the anionic redox, become crucial for both experimentalists and theorists. Using advanced experimental tools (e. g., synchrotron radiation technologies, transmission electron microscope, X-ray photoemission spectroscopy, and electron spin resonance) combined with density functional theory (DFT) calculations, three types of redox processes are revealed in the reported cathode materials with anionic redox including: 1) cationic redox first and anionic redox next, such as in layered NMC

[14,19,20]; 2) simultaneous cationic and anionic redox, such as in Li_5FeO_4 [29] and 3) anionic redox only, such as in Li_2MnO_3 [21-23], Li_8ZrO_6 [27], and Li_3IrO_4 [28]. Since most cathode materials are so-called charge-transfer materials, with the top valence bands contributed by transition metal-ligand hybridization, it is not quite surprising that the oxygen O-2*p* states close to the Fermi level facilitates the reversible oxygen redox to reach extra capacities. However, little is known about either when the anion redox is triggered in certain materials, or what is the physical origin behind the possible cation-anion redox transition. The answers to these questions in a theoretical perspective are challenging because especially for oxygen redox, the notorious self-interaction error (SIE) of standard DFT (or even DFT+U [35]) approach often leads to overestimated delocalization effect of the wavefunctions [36-38], and meanwhile, an unrealistic local geometry upon introducing addition carriers. Recently, DFT calculations with hybrid functional HSE06 (which could correct SIE to some extent) claimed that the oxygen redox is originated from Li/TM cationic disorder on the promotion of O-2*p* non-bonding orbitals at the Fermi level [15].

Using hybrid density functional study combined with the modern perspective of doping and experimental soft X-ray absorption spectroscopy (sXAS) measurements, we proved that $Li_{(2-x)}FeSiO_4$ (0

$< x <$ 2), performs sequent cation and anionic redox activity upon delithation. During delithiation, our results demonstrated that Fe^{2+} ions changes to Fe^{3+} till a critical Li concentration x = 1, while further Li extraction triggers oxygen redox instead of cation oxidation. This oxygen redox is reversible and stable until nearly 1.8 Li-ions extracted, corresponding to an extra capacity of 0.8 Li-ions induced by anionic redox activity. In order to uncover the physical origin of the exact transition point (x = 1) of cationic/anionic redox, we then focused on slight lithiation and delithiation behaviors of $LiFeSiO_4$. Interestingly, we found that both of lithiation and delithiation processes result in a polaronic state, but with cationic and anionic character, respectively. In contrast to the previous reported oxygen clustering during oxygen redox in Li-rich layered TM oxides, the oxygen polaron in $Li_{(2-x)}FeSiO_4$ is localized on a single O-ion, which avoids the peroxo-like O−O bond formation to prevent the lattice O loss. Moreover, we found that not all the polyoxyanion $Li_{(2-x)}TMSiO_4$ (TM = Mn, Fe, Co and Ni) exhibit such polaronic oxygen redox activity after more than one Li-ion extracted, but show a strong dependence on the 3d occupation numbers of TM. Specifically, Li_2MnSiO_4 shows the multiple cationic redox (Mn^{2+}-Mn^{4+}) during the whole delithiation; Li_2CoSiO_4 shows a simultaneous cationic and anionic redox with all oxygen ions participating the

charge transfer; and Li_2NiSiO_4 show the similar polaronic oxygen redox activity as Li_2FeSiO_4 after cation redox until 1 Li/f.u. extracted.

Results

Electrochemical performance of Li_2FeSiO_4. In the polyoxyanion-type intercalation $Li_{(2-x)}FeSiO_4$ structures, each iron, lithium, and silicon atom is coordinated by four oxygen atoms, while the FeO_4 tetrahedra are cross-linked by silicate groups. Based on the previous studies [39,40], two phase transformation happens from the initially prepared phase ($P2_1/n$ for prepared-Li_2FeSiO_4) to cycling stable phase (β_{II} phase, inversed-$Pmn2_1$) during the initial charge and discharge processes. Here we mainly focus on the latter structure for Li_2FeSiO_4 (Supplementary Fig. 1). The reversibility of lithiation/delithiation for Li_2FeSiO_4 compounds was examined versus Li in Swagelok cells cycled between 1.5 and 4.8 V at a 0.05 C rate (Fig. 1a). It can be seen that the 1st discharge specific capacity is 305 mAh/g, corresponding to 1.86 Li-storages per Li_2FeSiO_4 unit with oxygen redox happening, close to the previous reported performance of Li_2FeSiO_4 nanocrystals [41]. The initial charge curve showed two obvious voltage plateaus at 3.0 and 4.5 V and the 2nd curve was largely different from that of the 1st cycle. This phenomenon is ascribed to structural rearrangements involving the

exchange of lithium and iron between their sites during the 1st charge. Fig. 1b further illustrates the cycling performance conducted at 0.05 C for 50 cycles, and a retention of 88% was obtained after 50 cycles, revealing a relative stable long-term performance compared with the reported Li-rich TM oxides [10,16,26,29,30].

We note that almost all of the previous experimental [41-45] and theoretical studies [36,37] held that during the whole delithiation process in $Li_{(2-x)}FeSiO_4$, i.e., from $x = 0$ to $x = 2$, the cation valence $Fe^{2+} \rightarrow Fe^{3+} \rightarrow Fe^{4+}$ should account for the redox activity. Recently, Orikasa *et al.* performed sXAS measurements and reported that the difference in edge shift for the Fe *K*-edge X-ray absorption near edge structure (XANES) during the charging and discharging processes between $LiFeSiO_4$ and $FeSiO_4$ is very small, while the pre-edge peak for the XANES spectra at the O *K*-edge increases significantly when going from $LiFeSiO_4$ and $FeSiO_4$. Thus, it is concluded that during delithiation from $LiFeSiO_4$ to $FeSiO_4$, oxygen ligand holes are formed rather than $Fe^{3+} \rightarrow Fe^{4+}$ oxidation [46]. However, previous DFT studies (with standard exchange-correlation functionals and Hubbard-like U correction) even predict a metallic state for $Li_{(2-x)}FeSiO_4$ during delithiation [36,47], in sharp contrast to the semiconducting phase as reported by experiments [48,49]. Clearly, the uncertainty about the Fe valence state and whether there is an

oxygen redox activity is imperative for the full understanding of the whole delithiation process in Li_2FeSiO_4.

Sequent cation and anion redox in $Li_{(2-x)}FeSiO_4$. To reveal the underlying mechanism of the redox process during delithiation, we next perform DFT calculations to revisit different delithiation stages of $Li_{(2-x)}FeSiO_4$, and compare the results with our sXAS measurements. We apply hybrid functional in the form of Heyd–Scuseria–Ernzerhof (HSE06) [50], which mixes the exact exchange in Hartree-Fock theory with the semilocal exchange-correlation functionals to correct the SIE. The evolution of the density of states for the unit cell ($Li_4Fe_2Si_2O_8$) of partially delithiated $Li_{(2-x)}FeSiO_4$ (x = 0, 0.5, 1.0, and 1.5) is shown in Fig. 1a (the corresponding crystal structures is shown in Supplementary Fig. 2). It is found that when x goes from 0 to 1.5, the band gap E_g changes from 2.91 eV (x = 0) to 3.60 eV and 0.57 eV for x = 1 and x = 1.5, respectively, in sharp contrast with the previous DFT+U results [36,47] and consistent with the semiconducting phase as reported by experiments [48,49]. Our results naturally explain that $Li_{(2-x)}FeSiO_4$ always keeps a poor electronic conductivity and rate capability during electrochemical cycling [51]. From top three panels of Fig. 2a, we can see that the Fe-3*d* peak right below the Fermi level is gradually shifted upward after the first Li extraction per f.u., indicating the redox couple of

Fe^{2+}/Fe^{3+}. However, the second Li-ion extraction shifts valence states with pure O-2*p* character cross the Fermi level (Fig. 2a, bottom panel), indicating that instead of Fe^{3+}/Fe^{4+}, it is O anion playing an active role. Interestingly, the upward shifted O-2*p* states form a localized, polaron-like hole state inside the band gap of $LiFeSiO_4$. Such a hole-localized state is confirmed by the isosurface of the spin density of partially delithiated $Li_{(2-x)}FeSiO_4$ (x = 1 and 1.5), as shown in Fig. 2b. We observe large spin density from two oxygen ions with the shape of an isolated O-2*p* orbital for $Li_{0.5}FeSiO_4$, indicating that this polaron state is localized on two O ions belonging to one SiO_4 tetrahedron. The calculated magnetic moments of Fe and O in partially delithiated $Li_{(2-x)}FeSiO_4$ (Fig. 2c) also support the whole redox process analyzed above. From Li_2FeSiO_4 to $LiFeSiO_4$, the magnetic moments of the two Fe cations changes from 3.61 μB (Fe^{2+}, $e_g^3 t_{2g}^3$) to 4.17 μB (Fe^{3+}, $e_g^2 t_{2g}^3$) by sequence, indicating a cationic redox process. For the further delithiation (from x = 1 to x = 1.5), the magnetic moments of Fe ions keep nearly unchanged, while the magnetic moments of two O ions (unchanged from Li_2FeSiO_4 to $LiFeSiO_4$) start to change to -0.25 μB in $Li_{0.5}FeSiO_4$.

The structural response to the creation of hole polarons is shown in Fig. 2d. From Li_2FeSiO_4 to $LiFeSiO_4$, both of the Fe-O and Si-O

coordination remain tetrahedral symmetry, but the volumes shrink because of the losing electron, in agreement with the picture of cationic oxidation expected from the above results. For the sequent anionic oxidation process (from Li_1FeSiO_4 to $Li_{0.5}FeSiO_4$), the oxygen network is now strongly modified with symmetry breaking. Two Fe-O bonds (far from the extracted Li-ion) of the FeO_4 tetrahedra keep unchanged (1.88 Å), while for the other two Fe-O bonds next to the extracted Li-ion, one is shortened to 1.79 Å, but the other one shows longer bond length of 1.85 Å. Moreover, one of the six O–O distances of the SiO_4 tetrahedron decreases from ca. 2.70 Å in Li_1FeSiO_4 to ca. 2.32 Å in $Li_{0.5}FeSiO_4$. We note that these two adjacent O ions are just the localization centers of the hole-polaron state of $Li_{0.5}FeSiO_4$, indicating a $2O^{2-}/(O_2)^{3-}$ process, which is similar to the peroxo-like oxygen redox process in layered TM oxides [10,15-18,28].

To further confirm the above theoretical calculations, the Fe *L-edge* and O *K-edge* sXAS of samples Li_2FeSiO_4, Li_1FeSiO_4, and $Li_{0.15}FeSiO_4$ are tested, as shown in Fig. 3a and 3b, respectively. According to the previous study [52-54], the relation between the Fe *L*-edge spectra and the Fe oxidation state is well defined. Our results show that the Fe valence state of Li_1FeSiO_4, and $Li_{0.15}FeSiO_4$ are both nearly pure Fe^{3+}, which means that the balance of the Li- extraction

from Li_1FeSiO_4 to $Li_{0.15}FeSiO_4$ is not from the evolution of the Fe oxidation state. On the other hand, the O *K-edge* XAS difference between Li_1FeSiO_4 and $Li_{0.15}FeSiO_4$ has been clearly shown in Fig. 3b, in which a new feature located at 534 eV shows up for $Li_{0.15}FeSiO_4$ compared with the Li_1FeSiO_4. Such character indicates that the oxygen valence state would change to balance the Li-extraction from Li_1FeSiO_4 to Li_0FeSiO_4. We note that the 535.8 eV feature on the Li_2FeSiO_4 is likely related to the –OH bonding [55], which may be from the sample preparation progress. Our sXAS results are also in accordance with the previous reported experiment on $Li_{(2-x)}FeSiO_4$ [46], providing a solid support to the physical picture suggested by our theoretical calculations.

Cation/anion transition at the critical point $x = 1$. A general discussion on the origin of anionic redox activity in $Li_{(2-x)}FeSiO_4$ can be found in Supplementary Note 1. In the following, to get a microscopic picture on how the switch between cation and anion redox is triggered at the transition point $x = 1$ for $Li_{(2-x)}FeSiO_4$, we focused on lithiation and delithiation behaviors of $LiFeSiO_4$ at a small concentration, which corresponds to a doping perspective. The challenge of such prediction of dilute doping lies in that especially for delithiation, the localized hole states are often incorrectly described in standard DFT exchange-correlation functionals as

rather delocalized states that spread over all oxygen ligands [56-58]. Such “delocalization error [59]” originates from the convex bowing of the total energy $E(N)$ with respect to electron occupation number N, a manifestation of SIE leading to energy gain by *spreading* the wavefunction. Since Hartree-Fock theory exhibits concave bowing $E(N)$ versus N, hybrid functional with a predefined mixing parameter (0.25 is used here) can incompletely restore the linearity of $E(N)$. Indeed, a perfect correction is required to fulfill the so-called generalized Koopmans condition

$$\Delta_{nk} = E(N+1) - E(N) + eig(N) = 0, \quad (1)$$

where $E(N+1) - E(N)$ denotes ther total energy cost to add an electron from the hole-doped system, and $eig(N)$ the single-particle energy of the lowest unoccupied state in the electron-doped system. Here we use the Lany-Zunger approach [38] to restore the generalized Koopmans condition, by introducing a potential operator that acts only on the doping states within the DFT+U regime (parametrized by a single onsite potential coefficient λ_h, see Methods for details).

Starting from the cation/anion transition point (x = 1), we use a 2 × 2 × 2 supercell (16 Li atoms per cell) of $LiFeSiO_4$ and remove or add one Li atom to achieve a relative low carrier doping concentration (~ 6%). By removing one Li atom, the projected

density of states (PDOS) of $Li_{0.94}FeSiO_4$ (Fig. 4a, top panel) exhibits a localized O accepter state inside the fundamental band gap between Fe-like Hubbard band and O-like charge-transfer band, similar with $Li_{0.5}FeSiO_4$ (Fig. 2a). Note that here we choose λ_h to be λ_c = 4.5 eV, at which point the generalized Koopmans condition Eq. (1) is exactly fulfilled, i.e., Δ_{nk} = 0 (Fig. 4c). However, the charge density of the localized state (Fig. 4b) shows that the small oxygen polaron in $Li_{0.94}FeSiO_4$ is localized on a single O-ion, rather than a $(O_2)^{3-}$ cluster for high delithiation concentrations as discussed above and previous studies [10,15-18,28] or the recently reported large-size polaron in $(PbBr_3)^-$ based halide perovskites [60]. Such a scenario of single-O polaron is further verified by the structural and magnetic properties around the Li vacancy. As shown in Fig. 4d, when exceeds a critical value of 4.0 eV, a breaking of the tetrahedral symmetry occurs, evidenced by that one Fe-O^{1-} bond is apparently elongated compare with the other three Fe-O^{2-} bonds and so as Si-O bonds. In contrast, a standard DFT+U calculation (λ_h = 0) or with small λ_h predicts a high-symmetry extended acceptor state with an

equal amplitude of all Fe-O and Si-O bonds. The polaronic state also suggests the emergence of a local magnetic moment at the O^{1-} ion that traps the hole. Since our λ_h that fulfills Eq. (1) (4.5 eV) is higher than the transition value (4.0 eV), the stabilized single-O polaronic state is predicted to be the physical reality at the delithiation process with low concentration. This means that in $LiFeSiO_4$, delithiation starts by forming single-O^{1-} polaron, while the O clusters begin to form when an amount of elongated Fe-O bonds are close enough at a relatively high concentration (e.g., $x = 1.5$).

On the other hand, adding one Li to $LiFeSiO_4$ (leading to $Li_{1.06}FeSiO_4$) exhibits an electron polaron state dominated by Fe-3*d* orbitals, as shown in Fig. 4a (bottom panel). As a result, associated with this lithiation process, a Fe^{3+} ion is reduced to Fe^{2+}, corresponding to traditional cation redox activity. Note that we did not apply any onsite potential on the donor state here because similar to other Fe^{3+} system such as Fe_2O_3, DFT+U already satisfies the generalized Koopmans condition in good approximation [61]. Overall, by dilute doping approach we observe exact cation/anion redox transition at $LiFeSiO_4$ ($x = 1$), with the formation of electron/hole single polaron formation for the cation/anion redox process.

Redox activity in other $Li_{(2-x)}TMSiO_4$ compounds. We next consider other $Li_{(2-x)}TMSiO_4$ (TM = Mn, Co, and Ni) materials [36,62-66] to see whether the existence of oxygen redox activity is universal among these polyanionic materials. For $Li_{(2-x)}MnSiO_4$, PDOS plots show that upon delithiation from x = 0 up to x = 1.5 the cation valence Mn^{2+} → Mn^{3+} → Mn^{4+} accounts for the redox activity (Supplementary **Fig.** 4). It should be noted that there is also a small portion of oxygen redox activity accompanied with the main Mn redox. The calculated magnetic moments of Mn in partially delithiated $Li_{(2-x)}MnSiO_4$ also support the redox of Mn^{2+} → Mn^{3+} → Mn^{4+}, with the magnetic moment of Mn changing from 4.51 μB in Li_2MnSiO_4, to 3.69 μB in $LiMnSiO_4$, and finally to 2.83 μB in $Li_{0.5}MnSiO_4$ (Fig. 5a). In contrast, the magnetic moment of O keeps nearly unchanged, indicating the small portion of oxygen redox activity observed in the PDOS can be neglected (Fig. 5a). Similar to Li_2MnSiO_4, Li_2CoSiO_4 also exhibits the dominated cationic redox accompanied by a little degree of oxygen redox activity during the whole delithiation process (Supplementary Fig. 5). The only difference is that the oxygen redox in Li_2CoSiO_4 can't be neglected, as indicated from Fig. 5b that the magnetic moments of both O1 and O2 in Li_2CoSiO_4 increases from 0.04 to 0.26 μB from Li_2CoSiO_4 to $Li_{0.5}CoSiO_4$. While going to Li_2NiSiO_4, the redox process resembles

the case of Li_2FeSiO_4 again: Ni^{2+}/Ni^{3+} redox couple for the first Li-ion extraction (per f.u.) and polaron-like oxygen redox couple for the second Li-ion extraction (Supplementary Fig. 6). This is also supported by the calculated magnetic moments of Ni in partially delithiated $Li_{(2-x)}NiSiO_4$ (Fig. 5c), changing from 1.73 μB (Ni^{2+}, $e_g^4t_{2g}^4$) in Li_2NiSiO_4 to 2.11 μB (Ni^{3+}, $e_g^4t_{2g}^3$) in $LiNiSiO_4$ and then keeps nearly unchanged (2.11 μB for Ni in $Li_{0.5}NiSiO_4$). On the other hand, the magnetic moments of one O ion (O1) increase a little by 0.13 μB from Li_2NiSiO_4 to $LiNiSiO_4$ and then sharply change to -0.69 μB in $Li_{0.5}NiSiO_4$ (Fig. 5c). The isosurfaces of the spin density for the partially delithiated $Li_{(2-x)}TMSiO_4$ (x = 1 and 1.5) further confirm the above calculations: We observe no spin density for all the oxygen ions in $Li_{(2-x)}MnSiO_4$, nonzero spin density for all the oxygen ions in $Li_{(2-x)}CoSiO_4$, and large spin density with the shape of an isolated O-2p orbital on O1 in $Li_{0.5}NiSiO_4$ (Fig. 5d).

From the above results, we can conclude that the redox activity in $Li_{(2-x)}TMSiO_4$ (TM = Mn, Fe, Co and Ni) shows a strong dependence on the 3d occupation numbers of TM. Specifically, Li_2NiSiO_4 exhibits the same polaronic oxygen redox activity as Li_2FeSiO_4 after more than one Li-ion extracted, while Li_2MnSiO_4 shows the multiple cationic

redox (Mn^{2+}-Mn^{4+}) during the whole delithiation, Li_2CoSiO_4 shows a simultaneous cationic and anionic redox with the universal (but not equivalent) charge transfer on each oxygen ions. A detailed discussion on the evolution of energy orbitals during delithiation explaining the above differences of the redox activity for $Li_{(2-x)}TMSiO_4$ family is provided in Supplementary Note 2 and Note 3.

Discussion. We would like to comment the corresponding experimental capacity for different polyanionic materials with our calculations discussed above. Li_2MnSiO_4 is reported to show a high capacity of 290 mAh/g (corresponding to 1.7 Li per f.u.) at a discharge rate of 0.02 C (1 C = 333mA/g) [66], a little lower than Li_2FeSiO_4 with 305 mAh/g (corresponding to 1.86 Li per f.u.) at a discharge rate of 0.05 C, while Li_2CoSiO_4 only shows a capacity of 170 mAh/g (corresponding to 1.1 Li per f.u.) at a discharge rate of 0.03 C [62]. The high capacity of Li_2MnSiO_4 can be attributed to the multiple cationic redox (Mn^{2+}-Mn^{4+}) during the whole delithiation. So there is no significant charge transfer from lattice oxygen, which ensures the stability of lattice oxygen and also the whole structure stability during delithiation. For Li_2CoSiO_4, though the cationic redox accounts for the main activity during the whole delithiation process, the accompanied oxygen redox can’t be neglected. Unlike the sequent cationic and anionic redox process in Li_2FeSiO_4, it is more

like a simultaneous cationic and anionic redox in Li_2CoSiO_4 according to our calculations. Moreover, unlike Li_2FeSiO_4, the accompanied oxygen redox in Li_2CoSiO_4 doesn't show a polaronic state with one Li-ion extracted but show the universal charge transfer on every oxygen ions, which make it easy to form $(O_2)^{n-}$ ($0 < n < 4$) clusters. As a result, the loss of lattice oxygen would be easily triggered during delithiation, which explains that only 1.1 Li-ions can be delithiated for Li_2CoSiO_4.

As we know, Ni is widely accepted to be responsible for the main reactive species in layered Ni-containing oxides, acting as a double redox-active center [7,67-69] with $Ni^{2+} \rightarrow Ni^{3+} \rightarrow Ni^{4+}$. However, in our calculation of Li_2NiSiO_4, $Ni^{3+} \rightarrow Ni^{4+}$ is forbidden during the second Li-ion extraction. Although Li_2NiSiO_4 has never been reported to be synthesized successfully, our results suggest that it would be interesting to revisit the validity of the double redox-activity for Ni in layered Ni-containing oxides in the future.

To summarize, by systematical study of the delithiation process of $Li_{(2-x)}FeSiO_4$ with the combination of first-principle calculations and sXAS measurements, we demonstrated a reversible sequent cationic and anionic redox process in $Li_{(2-x)}FeSiO_4$. Namely, the first Li-ion extraction (per f.u.) is attributed to the cation valence change from Fe^{2+} to Fe^{3+}, while the second Li-ion extraction activates almost

exclusively the oxygen redox. This full delithiation is reversible and stable until nearly 1.8 Li-ions extracted, corresponding to an extra capacity of 0.8 Li-ions induced by anionic redox activity. We then focused on slight lithiation and delithiation behaviors of $LiFeSiO_4$ in a doping perspective and demonstrated the exact transition point of cation/anion redox at $LiFeSiO_4$ (x = 1). Interestingly, both of the lithiation and delithiation processes around the transition point result in electron and hole polaronic states with cationic and anionic character, respectively. In contrast to the previous reported oxygen clustering in Li-rich layered TM oxides, the oxygen polaron in $Li_{(2-x)}FeSiO_4$ is localized on a single O-ion when the anion redox is triggered. Finally, the series of polyoxyanion $Li_{(2-x)}TMSiO_4$ (TM = Mn, Fe, Co and Ni) compounds do not exhibit a universal feature of oxygen redox in general, but a dependence on the 3d occupation numbers of TM. This work provides new insights of the anionic redox activity in the traditional polyanionic cathode materials, and paves the way for the future design of high-capacity rechargeable batteries.

Methods

First-principles calculations. All DFT calculations are performed using the plane-wave projector-augmented wave method [70,71], as

implemented in the Vienna *ab initio* simulation package [72,73]. The initial supercell is built according to the experimentally measured lattice constants [49]. Then it is fully optimized (including atomic positions and lattices) to get the Li_2FeSiO_4 structure. The $Li_{(2-x)}FeSiO_4$ structures were obtained by fully optimizing the Li_2FeSiO_4 structures with different degrees of delithiation. To obtain reliable optimized structures, the maximum residual force is less than 0.01 eV/Å and energies are converged to within 10^{-5} eV per atom. An energy cut-off of 520 eV was used in all cases. A ferromagnetic high-spin Fe state is assumed, and the energetic effects of the magnetic ordering are very small (below 0.005 eV per formula).

To predict the realistic behavior of the polyanionic cathode materials, we applied two different methods to correct the self-interaction errors. For $Li_{(2-x)}TMSiO_4$ (two TM atoms per cell), hybrid functional calculations with the form of Heyd–Scuseria–Ernzerhof (HSE06) [50] is employed, in which 25% Fock exchange is used in both structure optimization and electronic structure calculations. For the lithiation/delithiation process with a dilute concentration, we use a 2×2×2 supercell (16 TM atoms per cell) and add electron potentials on certain *lm* decomposed orbitals on top of the DFT+U framework, in which the Dudarev's approach [74] is used for Fe-d states ($U - J = 4$ eV). The onsite potential is implemented as the combination of

DFT+U and non-local external potentials method from Ref. [75]. For hole doping, the corresponding electron state potential is given by

$$V_h = \lambda_h (1 - n_{m,\sigma}/n_{host}), \quad (2)$$

where $n_{m,\sigma}$ and n_{host} denote the occupation of the m sublevel of spin σ, and the occupation of the host material without doping. We determine n_{host} in Eq. (2) to be 0.595 from the partial charge of the O-p orbitals of the occupied states. The parameter λ_h is tuned to perfectly fulfil the linearity of $E(N)$, i.e., the generalized Koopmans condition Eq. (1). For charged states, the image charge corrections due to the periodic supercells are considered by using the method of Lany and Zunger [76]. The comparison of results between hybrid functional and Lanyu-Zunger approach is shown in Supplementary Note 4.

Soft X-ray Spectroscopy (sXAS). The Fe L-edge and O K-edge X-ray absorption spectroscopy (XAS) on $Li_{2-x}FeSiO_4$ (x = 0, 1, and 2) were both performed at beamline 8.0.1 of the Advanced Light Source (ALS) at Lawrence Berkeley National Laboratory (LBNL). The undulator and spherical grating monochromator supplied a linearly polarized photon beam with resolving power up to 6000. The

experimental energy resolution was better than 0.15 eV. All the XAS experiments were performed at room temperature. All the spectra were collected in the total electron yield (TEY). All the spectra were normalized to the photon flux measured by the photocurrent of an upstream gold mesh.

Synthesis of Li_2FeSiO_4. lithium acetate (1.02 g), ferric nitrate (2.02 g), tetraethoxysilane (1.32 g), graphene oxide (50 mg) and P123 (1.00 g) were dissolved in ~100 ml ethanol/water mixed solution and then transferred to Teflon lined stainless steel autoclave and heated at 140 °C for 24 h to form precursor. Subsequently, the precursor was dried at 100 °C and then heated at 600 °C for 9 h under Ar to obtain Li_2FeSiO_4 sample.

Electrochemical measurements. The battery performance was tested with coin cells assembled in a glove box filled with pure argon. Lithium pellet was used as the anodes, a 1.0 M solution of $LiPF_6$ in ethylene carbonate/dimethyl carbonate (1/1) (bought from Shenzhen new main bond technology co., LTD. China) was used as the electrolyte, and the cathode electrodes were produced with 75% active material, 15% conducting agent (Ketjen Black) and 10% poly(tetrafluoroethylene) binder. Galvanostatic charge/discharge measurement was performed in the potential range from 1.5 to 4.8 V vs. Li/Li^+.

REFERENCES

1. Raebiger, H., Lany, S. & Zunger, A. Charge self-regulation upon changing the oxidation state of transition metals in insulators. *Nature* **453**, 763 (2008).
2. Cotton, A. F., Wilkinson, G., Bochmann, M. & Murillo, C. A. *Advanced Inorganic Chemistry*. (Wiley, 1999).
3. Wells, A. F. *Structural Inorganic Chemistry*. (Oxford University Press, 2012).
4. Goodenough, J. B. & Kim, Y. Challenges for rechargeable Li batteries. *Chem. Mater.* **22**, 587-603 (2009).
5. Lu, Z., MacNeil, D. & Dahn, J. Layered cathode materials $Li[Ni_xLi_{(1/3-\ 2x/3)}Mn_{(2/3-\ x/3)}]O_2$ for lithium-ion batteries. *Electrochem. Solid-State Lett.* **4**, A191-A194 (2001).
6. Ohzuku, T., Ueda, A., Nagayama, M., Iwakoshi, Y. & Komori, H. Comparative study of $LiCoO_2$, $LiNi_{12}Co_{12}O_2$ and $LiNiO_2$ for 4 volt secondary lithium cells. *Electrochimica Acta* **38**, 1159-1167 (1993).
7. Ren, H. *et al.* Effects of different carbonate precipitators on $LiNi_{1/3}Co_{1/3}Mn_{1/3}O_2$ morphology and electrochemical performance. *Mater. Chem. Phys.* **117**, 41-45 (2009).
8. Mizushima, K., Jones, P., Wiseman, P. & Goodenough, J. B. $LixCoO_2$ (0< x<-1): A new cathode material for batteries of high energy density. *Mater. Res. Bull.* **15**, 783-789 (1980).
9. Sathiya, M. *et al.* Reversible anionic redox chemistry in high-capacity layered-oxide electrodes. *Nat. Mater.* **12**, 827 (2013).
10. McCalla, E. *et al.* Visualization of OO peroxo-like dimers in high-capacity layered oxides for Li-ion batteries. *Science* **350**, 1516-1521 (2015).
11. McCalla, E. *et al.* Understanding the roles of anionic redox and oxygen release during electrochemical cycling of lithium-rich layered Li_4FeSbO_6. *J. Am. Chem. Soc.* **137**, 4804-4814 (2015).
12. Sathiya, M. *et al.* Electron paramagnetic resonance imaging for real-time monitoring of Li-ion batteries. *Nat. Commun.* **6**, 6276 (2015).
13. Grimaud, A., Hong, W., Shao-Horn, Y. & Tarascon, J.-M. Anionic redox processes for electrochemical devices. *Nat. Mater.* **15**, 121-126 (2016).
14. Luo, K. *et al.* Charge-compensation in 3d-transition-metal-oxide intercalation cathodes through the generation of localized electron holes on oxygen. *Nat. Chem.* **8**, 684-691 (2016).

15. Seo, D.-H. *et al.* The structural and chemical origin of the oxygen redox activity in layered and cation-disordered Li-excess cathode materials. *Nat. Chem.* **8**, 692-697 (2016).
16. Pearce, P. E. *et al.* Evidence for anionic redox activity in a tridimensional-ordered Li-rich positive electrode [beta]-Li_2IrO_3. *Nat. Mater.* **16**, 580-586 (2017).
17. Saubanère, M., McCalla, E., Tarascon, J.-M. & Doublet, M.-L. The intriguing question of anionic redox in high-energy density cathodes for Li-ion batteries. *Energ Environ Sci* **9**, 984-991 (2016).
18. Xie, Y., Saubanère, M. & Doublet, M.-L. Requirements for reversible extra-capacity in Li-rich layered oxides for Li-ion batteries. *Energ Environ Sci* **10**, 266-274 (2017).
19. Koga, H. *et al.* Reversible oxygen participation to the redox processes revealed for $Li_{1.20}Mn_{0.54}Co_{0.13}Ni_{0.13}O_2$. *J. Electrochem. Soc.* **160**, A786-A792 (2013).
20. Oishi, M. *et al.* Direct observation of reversible charge compensation by oxygen ion in Li-rich manganese layered oxide positive electrode material, $Li_{1.16}Ni_{0.15}Co_{0.19}Mn_{0.50}O_2$. *J. Power Sources* **276**, 89-94 (2015).
21. Chen, H. & Islam, M. S. Lithium extraction mechanism in Li-rich Li_2MnO_3 involving oxygen hole formation and dimerization. *Chem. Mater.* **28**, 6656-6663 (2016).
22. Xiao, R., Li, H. & Chen, L. Density functional investigation on Li_2MnO_3. *Chem. Mater.* **24**, 4242-4251 (2012).
23. Oishi, M. *et al.* Direct observation of reversible oxygen anion redox reaction in Li-rich manganese oxide, Li_2MnO_3, studied by soft X-ray absorption spectroscopy. *J. Mater. Chem. A* **4**, 9293-9302 (2016).
24. Luo, K. *et al.* Anion redox chemistry in the cobalt free 3d transition metal oxide intercalation electrode $Li[Li_{0.2}Ni_{0.2}Mn_{0.6}]O_2$. *J. Am. Chem. Soc.* **138**, 11211-11218 (2016).
25. Yabuuchi, N. *et al.* High-capacity electrode materials for rechargeable lithium batteries: Li_3NbO_4-based system with cation-disordered rocksalt structure. *P. Natl. Acad. Sci. USA* **112**, 7650-7655 (2015).
26. Yabuuchi, N. *et al.* Origin of stabilization and destabilization in solid-state redox reaction of oxide ions for lithium-ion batteries. *Nat. Commun.* **7**, 13814 (2016).
27. Huang, S. *et al.* Y-doped Li_8ZrO_6: A Li-Ion battery cathode material with high capacity. *J. Am. Chem. Soc.* **137**, 10992-11003 (2015).

28. Perez, A. J. *et al.* Approaching the limits of cationic and anionic electrochemical activity with the Li-rich layered rocksalt Li_3IrO_4. *Nat. Energy* **2**, 954 (2017).
29. Zhan, C. *et al.* Enabling the high capacity of lithium-rich anti-fluorite lithium iron oxide by simultaneous anionic and cationic redox. *Nat. Energy* **2**, 963 (2017).
30. Freire, M. *et al.* A new active Li-Mn-O compound for high energy density Li-ion batteries. *Nat. Mater.* **15**, 173-177 (2016).
31. Fang, C. *et al.* A Metal–organic compound as cathode material with superhigh capacity achieved by reversible cationic and anionic redox chemistry for high-energy sodium-ion batteries. *Angew. Chem. Int Edit.* **129**, 6897-6901 (2017).
32. Jung, S.-K. & Kang, K. Simultaneous anionic and cationic redox. *Nat. Energy* **2**, 912 (2017).
33. Li, B. & Xia, D. Anionic redox in rechargeable lithium batteries. *Adv. Mater.* (2017).
34. Lee, E. & Persson, K. A. Structural and chemical evolution of the layered Li-excess Li_xMnO_3 as a function of Li content from first-principles calculations. *Adv. Energy Mater.* **4**, 1400498 (2014).
35. Anisimov, V. I., Zaanen, J. & Andersen, O. K. Band theory and Mott insulators: Hubbard U instead of Stoner I. *Phys. Rev. B* **44**, 943 (1991).
36. Wu, S. Q., Zhu, Z. Z., Yang, Y. & Hou, Z. F. Structural stabilities, electronic structures and lithium deintercalation in Li_xMSiO_4 (M=Mn, Fe, Co, Ni): A GGA and GGA+U study. *Comput. Mater. Sci.* **44**, 1243-1251 (2009).
37. Zhang, P., Hu, C., Wu, S., Zhu, Z. & Yang, Y. Structural properties and energetics of Li_2FeSiO_4 polymorphs and their delithiated products from first-principles. *Phys. Chem. Chem. Phys.* **14**, 7346-7351 (2012).
38. Lany, S. & Zunger, A. Polaronic hole localization and multiple hole binding of acceptors in oxide wide-gap semiconductors. *Phys. Rev. B* **80**, 085202 (2009).
39. Nytén, A., Kamali, S., Häggström, L., Gustafsson, T. & Thomas, J. O. The lithium extraction/insertion mechanism in Li_2FeSiO_4. *J. Mater. Chem.* **16**, 2266-2272 (2006).
40. Sirisopanaporn, C., Masquelier, C., Bruce, P. G., Armstrong, A. R. & Dominko, R. Dependence of Li_2FeSiO_4 electrochemistry on structure. *J. Am. Chem. Soc.* **133**, 1263-1265 (2010).
41. Yang, J. *et al.* Graphene activated 3D-hierarchical flower-like Li_2FeSiO_4 for high-performance lithium-ion batteries. *J. Mater. Chem. A* **3**, 16567-16573 (2015).

42. Wu, X., Jiang, X., Huo, Q. & Zhang, Y. Facile synthesis of Li_2FeSiO_4/C composites with triblock copolymer P123 and their application as cathode materials for lithium ion batteries. *Electrochimica Acta* **80**, 50-55 (2012).
43. Kamon-in, O. *et al.* A study of transient phase transformation in LFS/C using in-situ time resolved X-ray absorption spectroscopy. *Int. J. Electrochem. Sci* **9**, 4257-4267 (2014).
44. Lv, D. *et al.* A novel Li_2FeSiO_4/C composite: Synthesis, characterization and high storage capacity. *J. Mater. Chem.* **21**, 9506-9512 (2011).
45. Zhao, Y. *et al.* In situ generation of Li_2FeSiO_4 coating on MWNT as a high rate cathode material for lithium ion batteries. *J. Mater. Chem.* **22**, 18797-18800 (2012).
46. Masese, T. *et al.* Crystal structural changes and charge compensation mechanism during two lithium extraction/insertion between Li_2FeSiO_4 and $FeSiO_4$. *J. Phys. Chem. C* **119**, 10206-10211 (2015).
47. Li, Y., Cheng, X. & Zhang, Y. Achieving high capacity by vanadium substitution into Li_2FeSiO_4. *J. Electrochem. Soc.* **159**, A69-A74 (2012).
48. Kokalj, A. *et al.* Beyond one-electron reaction in Li cathode materials: designing $Li_2Mn_xFe_{1-x}SiO_4$. *Chem. Mater.* **19**, 3633-3640 (2007).
49. Yang, J. L. *et al.* Tuning structural stability and lithium-storage properties by d-orbital hybridization substitution in full tetrahedron Li_2FeSiO_4 nanocrystal. *Nano Energy* **20**, 117-125 (2016).
50. Heyd, J., Scuseria, G. E. & Ernzerhof, M. Hybrid functionals based on a screened Coulomb potential. *J. Chem. Phys.* **118**, 8207-8215 (2003).
51. Nishimura, S.-i. *et al.* Structure of Li_2FeSiO_4. *J. Am. Chem. Soc.* **130**, 13212-13213 (2008).
52. Zhuo, Z., Hu, J., Duan, Y., Yang, W. & Pan, F. Transition metal redox and Mn disproportional reaction in LiMn0.5Fe0.5PO4 electrodes cycled with aqueous electrolyte. *Appl. Phys. Lett.* **109**, 023901 (2016).
53. Liu, X. *et al.* Phase Transformation and Lithiation Effect on Electronic Structure of LixFePO4: An In-Depth Study by Soft X-ray and Simulations. *J. Am. Chem. Soc.* **134**, 13708-13715 (2012).
54. Li, Q. *et al.* Quantitative probe of the transition metal redox in battery electrodes through soft x-ray absorption spectroscopy. *J. Phys. D: Appl. Phys.* **49**, 413003 (2016).

55. Wernet, P. *et al.* The Structure of the First Coordination Shell in Liquid Water. *Science* **304**, 995-999 (2004).
56. Pacchioni, G., Frigoli, F., Ricci, D. & Weil, J. A. Theoretical description of hole localization in a quartz Al center: The importance of exact electron exchange. *Phys. Rev. B* **63**, 054102 (2000).
57. Chan, J. A., Lany, S. & Zunger, A. Electronic correlation in anion *p* orbitals impedes ferromagnetism due to cation vacancies in Zn chalcogenides. *Phys. Rev. Lett.* **103**, 016404 (2009).
58. Lægsgaard, J. & Stokbro, K. Hole trapping at Al impurities in silica: a challenge for density functional theories. *Phys. Rev. Lett.* **86**, 2834-2837 (2001).
59. Mori-Sánchez, P., Cohen, A. J. & Yang, W. Localization and delocalization errors in density functional theory and implications for band-gap prediction. *Phys. Rev. Lett.* **100**, 146401 (2008).
60. Miyata, K. *et al.* Large polarons in lead halide perovskites. *Sci. Adv.* **3**, e1701217 (2017).
61. Peng, H. & Lany, S. Semiconducting transition-metal oxides based on d 5 cations: Theory for MnO and Fe_2O_3. *Phys. Rev. B* **85**, 201202 (2012).
62. Lyness, C., Delobel, B., Armstrong, A. R. & Bruce, P. G. The lithium intercalation compound Li2CoSiO4 and its behaviour as a positive electrode for lithium batteries. *Chem. Commun.*, 4890-4892 (2007).
63. Armstrong, A. R., Lyness, C., Ménétrier, M. & Bruce, P. G. Structural polymorphism in Li_2CoSiO_4 intercalation electrodes: a combined diffraction and NMR study. *Chem. Mater.* **22**, 1892-1900 (2010).
64. Gong, Z., Li, Y. & Yang, Y. Synthesis and electrochemical performance of Li_2CoSiO_4 as cathode material for lithium ion batteries. *J. Power Sources* **174**, 524-527 (2007).
65. Gummow, R. & He, Y. Recent progress in the development of Li_2MnSiO_4 cathode materials. *J. Power Sources* **253**, 315-331 (2014).
66. Yang, X.-F., Yang, J.-H., Zaghib, K., Trudeau, M. L. & Ying, J. Y. Synthesis of phase-pure Li_2MnSiO_4@ C porous nanoboxes for high-capacity Li-ion battery cathodes. *Nano Energy* **12**, 305-313 (2015).
67. Hwang, B. J., Tsai, Y. W., Carlier, D. & Ceder, G. A combined computational/experimental study on $LiNi_{1/3}Co_{1/3}Mn_{1/3}O_2$. *Chem. Mater.* **15**, 3676-3682 (2003).

68. Wu, Z. Z. *et al.* Depolarized and fully active cathode based on $Li(Ni_{0.5}Co_{0.2}Mn_{0.3})O_2$ embedded in carbon nanotube network for advanced batteries. *Nano Lett* **14**, 4700-4706 (2014).
69. Yu, H. J. *et al.* Study of the lithium/nickel ions exchange in the layered $LiNi_{0.42}Mn_{0.42}Co_{0.16}O_2$ cathode material for lithium ion batteries: experimental and first-principles calculations. *Energ Environ Sci* **7**, 1068-1078 (2014).
70. Blöchl, P. E. Projector augmented-wave method. *Phys. Rev. B* **50**, 17953-17979 (1994).
71. Kresse, G. & Joubert, D. From ultrasoft pseudopotentials to the projector augmented-wave method. *Phys. Rev. B* **59**, 1758-1775 (1999).
72. Kresse, G. & Furthmüller, J. Efficient iterative schemes for ab initio total-energy calculations using a plane-wave basis set. *Phys. Rev. B* **54**, 11169-11186 (1996).
73. Kresse, G. & Furthmuller, J. Efficiency of ab-initio total energy calculations for metals and semiconductors using a plane-wave basis set. *Comput. Mater. Sci.* **6**, 15-50 (1996).
74. Dudarev, S., Botton, G., Savrasov, S., Humphreys, C. & Sutton, A. Electron-energy-loss spectra and the structural stability of nickel oxide: An LSDA+ U study. *Phys. Rev. B* **57**, 1505 (1998).
75. Lany, S., Raebiger, H. & Zunger, A. Magnetic interactions of Cr− Cr and Co− Co impurity pairs in ZnO within a band-gap corrected density functional approach. *Phys. Rev. B* **77**, 241201 (2008).
76. Lany, S. & Zunger, A. Assessment of correction methods for the band-gap problem and for finite-size effects in supercell defect calculations: Case studies for ZnO and GaAs. *Phys. Rev. B* **78**, 235104 (2008).

Acknowledgement

This work was financially supported by the National Natural Science Foundation of China (No. 21603007 and 51602009), National Materials Genome Project (2016YFB0700600), and Shenzhen Science and Technology Research Grant (No. JCYJ20150729111733470 and JCYJ20151015162256516). Q. L. was supported by the National Young 1000 Talents Plan.

Additional information

Supplementary information is available in the online version of the paper. Reprints and permissions information is available online at www.nature.com/reprints. Correspondence and requests for materials should be addressed to J.Z., Q.L. and F.P..

Author contributions

J.Z., Q.L., and F.P. planned the project, supervised all aspects of the research, contributed to the main theory and to writing the manuscript. G.T., M.X. and Q.L. performed DFT calculations. J.Y. synthesized the Li_2FeSiO_4 samples and performed electrochemical experiments. Z.Z. performed sXAS tests. J.Z., G.T., M.X., Z.Z., W.Y., Q.L. and F.P. analyzed the data. J.Z. and Q.L. drafted the paper, and all authors revised it.

Competing financial interests

The authors declare no competing financial interests.

Figures and Captions

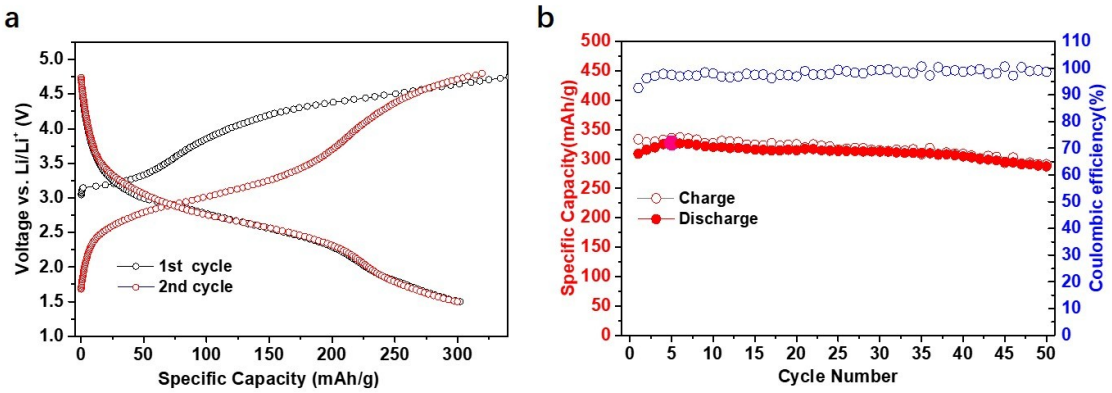

Figure 1. Electrochemical performance of Li_2FeSiO_4 nanoparticles. (a) Discharge–charge curves at a current rate of 0.1 C (1 C = 333mA/g). **(b)** Cycling performance at 0.1 C.

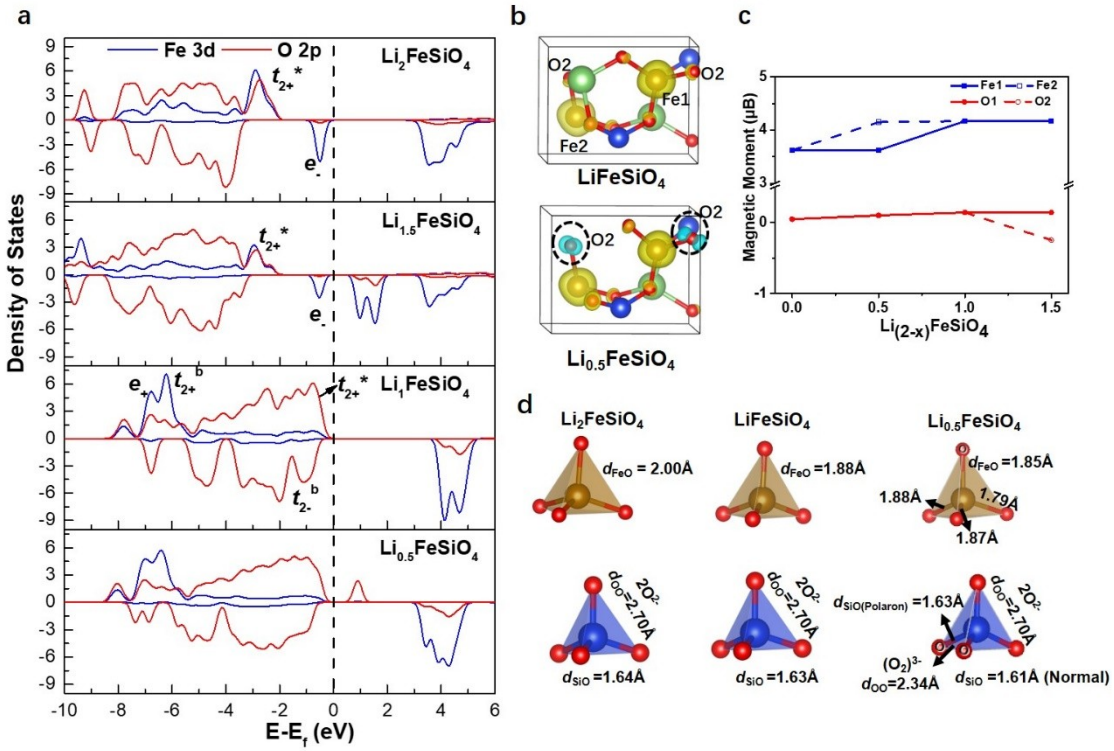

Figure 2. HSE calculated electronic structures for $Li_{(2-x)}FeSiO_4$ during delithiation. (a) Projected density of states (PDOS) of Fe-

3*d* and O-2*p* states in $Li_{(2-x)}FeSiO_4$ (x = 0, 0.5, 1.0, and 1.5). **(b)** The isosurface of the spin density in the unit cell of partially delithiated $Li_{(2-x)}FeSiO_4$ (x = 1.0 and 0.5). Green, Li; red, O; dark blue, Si; brown, Fe. The isovalues for the isosurfaces of the spin densities were 0.05 e $Å^{-3}$ for all cases. **(c)** The calculated magnetic moment of Fe and O in $Li_{(2-x)}FeSiO_4$ at different delithiation states. O1 and O2 denote two kinds of O ions with different variations of magnetic moment in $Li_{(2-x)}FeSiO_4$. O2 are denoted in (**b**), and all the left unidentified O ions in (**b**) are O1. **(d)** Direct visualization of oxo to peroxo $2O^{2-}/(O_2)^{n-}$ transformation upon delithiation: local environment of the Fe and Si cations (O–O distances and average Fe–O and Si-O distances).

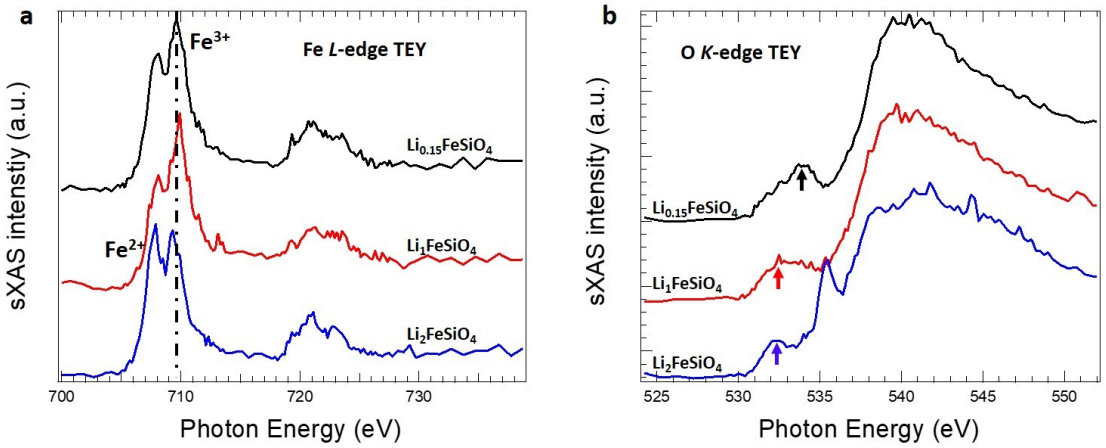

Figure 3. The Fe *L-edge* and O *K-edge* XAS on samples of Li_2FeSiO_4, Li_1FeSiO_4, and $Li_{0.15}FeSiO_4$.

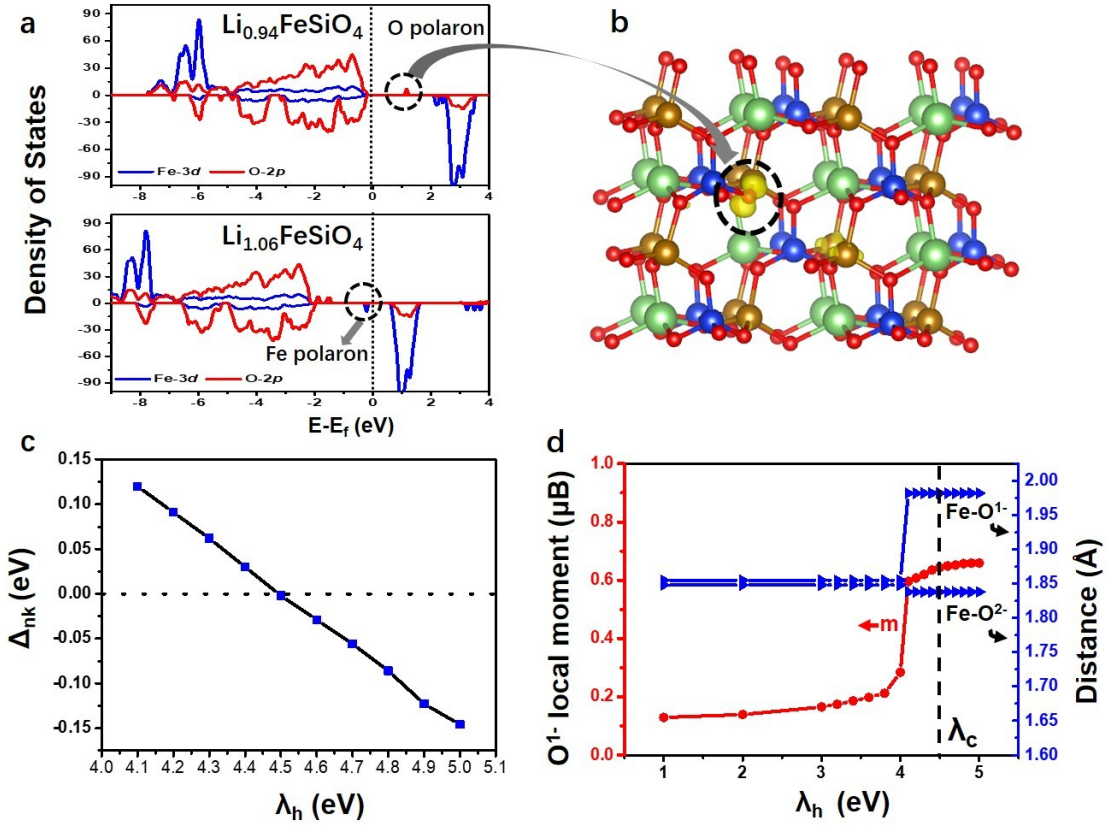

Figure 4. Cation/anion transition at the critical point $x = 1$. **(a)** PDOS of Fe-3*d* and O-2*p* states in $Li_{15}Fe_{16}Si_{16}O_{64}$ (delithiation, top panel) and $Li_{17}Fe_{16}Si_{16}O_{64}$ (lithiation, bottom panel). **(b)** The isosurface of the charge density of the O polaron state in the cell of $Li_{15}Fe_{16}Si_{16}O_{64}$, showing localization on a single O ion. **(c)** The electron addition energy $E_{add}=E(N+1)-E(N)$ and the energy eigenvalue $e_i(N)$ of the initially unoccupied acceptor state of Li. **(d)** Structural and magnetic properties of the O^{1-} in $Li_{15}Fe_{16}Si_{16}O_{64}$, as a function of the hole-state potential strength λ_h. The polaronic state

is stable above a value λ_h > 4.0 eV, while the critical value λ_c that fulfills the generalized Koopmans theory is marked by the dashed line. *m*: local magnetic moment of O^{1-}.

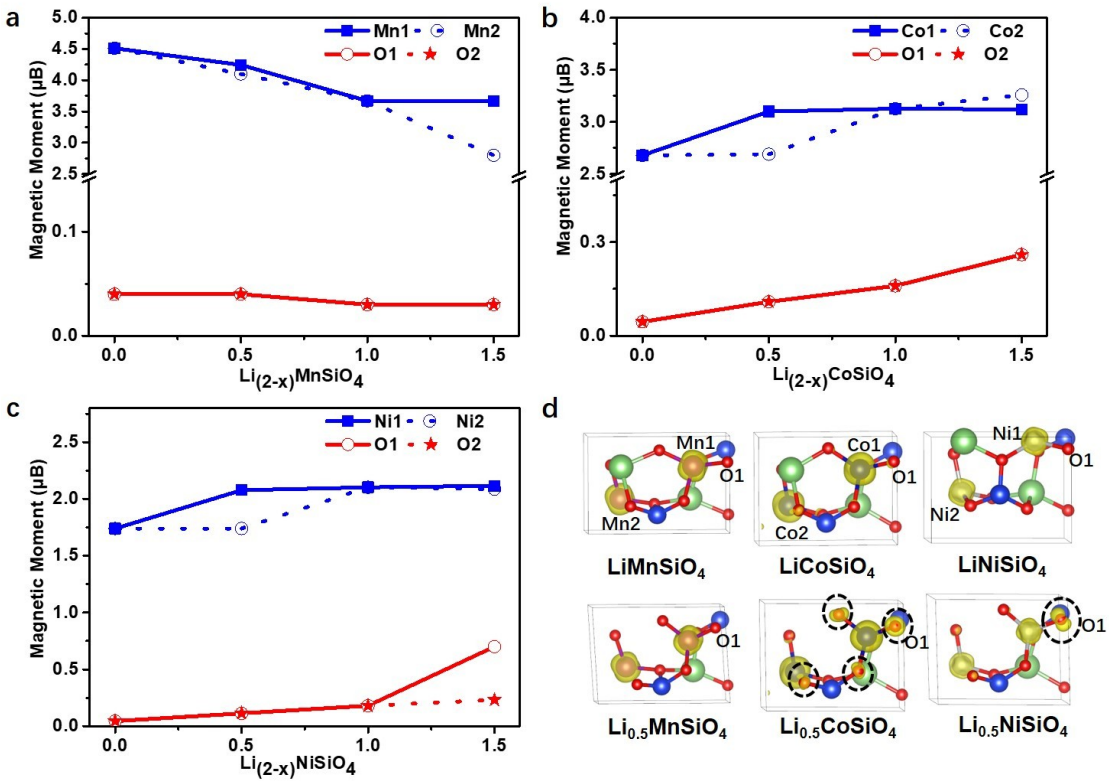
a
Mn1
Mn2
O1
O2
Magnetic Moment (μB)
Li(2-x)MnSiO4
b
Co1
Co2
O1
O2
Magnetic Moment (μB)
Li(2-x)CoSiO4
c
Ni1
Ni2
O1
O2
Magnetic Moment (μB)
Li(2-x)NiSiO4
d
Mn1
O1
Mn2
LiMnSiO4
Co1
O1
Co2
LiCoSiO4
Ni1
O1
Ni2
LiNiSiO4
O1
Li0.5MnSiO4
O1
Li0.5CoSiO4
O1
Li0.5NiSiO4

Figure 5. Redox activity in other $Li_{(2-x)}TMSiO_4$ compounds. (a to c) The calculated magnetic moment of TM and O in $Li_{(2-x)}TMSiO_4$ (TM = Mn, Co, and Ni) at different delithiation states. O1 are denoted in (**d**), and all the left unidentified O ions in (**d**) are O2. **(d)** The isosurface of the spin density in the unit cell of partially delithiated $Li_{(2-x)}TMSiO_4$ (x = 1.0 and 0.5). Green, Li; red, O; dark blue, Si; purple, Mn; light blue, Co; silver, Ni.